

Parametric 3D Convolutional Autoencoder for the Prediction of Flow Fields in a Bed Configuration of Hot Particles

Ali Mjalled¹, Reza Namdar², Lucas Reineking¹,
Mohammad Norouzi², Fathollah Varnik², Martin Mönnigmann¹

¹ Automatic Control and Systems Theory, Ruhr-Universität Bochum, Universitätsstraße 150, Bochum, 44801, Germany

² Interdisciplinary Centre for Advanced Materials Simulation, Ruhr-Universität Bochum, Universitätsstraße 150, Bochum, 44801, Germany

Abstract

The use of deep learning methods for modeling fluid flow has drawn a lot of attention in the past few years. Here we present a data-driven reduced model for predicting flow fields in a bed configuration of hot particles. The reduced model consists of a parametric 3D convolutional autoencoder. The neural network architecture comprises two main components. The first part resolves the spatial and temporal dependencies present in the input sequence, while the second part of the architecture is responsible for predicting the solution at the subsequent timestep based on the information gathered from the preceding part. We also propose the utilization of a post-processing non-trainable output layer following the decoding path to incorporate the physical knowledge, e.g., no-slip condition, into the prediction. The reduced model is evaluated by comparing the predicted solutions of the reduced model with the high-fidelity counterparts. In addition, proper orthogonal decomposition is employed to systematically analyze and compare the dominant structures present in both sets of solutions. The assessment of the reduced model for a bed configuration with variable particle temperature showed accurate results at a fraction of the computational cost required by traditional numerical simulation methods.

Keywords: Reduced model, Lattice Boltzmann, Neural networks, Autoencoder

1 Introduction

Over the past few decades, numerous experimental and numerical studies have been conducted to understand the flow behavior and heat transfer of fluids around solid bodies. Within this broad spectrum of research, great emphasis has been given to flow fields in packed beds, where the transfer of heat, mass and momentum are increased by providing an extended interfacial surface between the fluid and solid bodies. Packed beds play a crucial

role in a variety of areas, ranging from chemical processing such as separation (Bader et al., 2015), absorption (Lin et al., 2003) and catalytic processes (Ambrosetti et al., 2020) to energy storage applications like sensible heat storage systems (Elouali et al., 2019), and advanced adiabatic compressed air energy storage (Geissbühler et al., 2018). This wide range of applications as well as the effect of transfer phenomena on process efficiency, product quality and environmental sustainability (Bird, 2002), motivate investigating the key features of packed beds such as flow field, pressure drop, packing material, bed height, and packing density to ensure optimal performance.

Numerical methods are one of the most effective tools for analyzing the behavior of packed beds and optimizing their design parameters. The discrete element method (DEM), computational fluid dynamics (CFD) and the lattice Boltzmann method (LBM) are some of the common approaches that have been used to simulate packed bed configurations. DEM simulations have been applied to examine both the geometrical features of the packed beds and the movement of particles within them. For example, Kou et al. (2020) used DEM to examine the effect of shape, restitution coefficient, sliding coefficient, rolling coefficient, and diameter ratio of cubical particles on the behavior of the packed beds. CFD simulations, on the other hand, can capture the detailed flow field within the bed and the interaction between the fluid and particles. Kutscherauer et al. (2022) investigated flow field and heat transfer for a slender packed bed under various conditions. Moreover, a combination of different methods can be adopted. Bai et al. (2009) used a coupled DEM-CFD model to study flow field and pressure drop in fixed bed reactors. LBM, which is a relatively a new numerical method, has been utilized to simulate the interactions between fluid and particles, as well as the chemical reactions occurring within packed beds. Qi et al. (2019), for example, used LBM to investigate non-Newtonian fluid flow through a packed bed of uniform spheres.

The aforementioned numerical methods offer a more efficient and cost-effective alternative to experimental analysis for modeling diverse, packed bed configurations with varying properties. However, simulating large-scale packed beds using these methods requires substantial computational resources, making it a time-consuming and expensive process. Even with highly parallelizable techniques such as LBM, the simulation of large and complex packed beds can be limited, particularly when it comes to optimization problems.

In this context, building reduced models for packed bed simulations is an essential step toward reducing the computational cost and allowing for sensitivity analysis. The majority of model reduction approaches rely on mapping the high dimensional space into a smaller one on which the reduced model is defined. One of the most commonly employed methods in this context is based on proper orthogonal decomposition (POD) followed by a Galerkin projection (see, e.g., Benner et al. (2015), for a survey, and Reineking et al. (2023) for an engineering application). This method uses POD to extract a set of dominant modes that serve as a basis for the reduced space. Subsequently, Galerkin projection is employed to extract a small number (order of ten) of ordinary differential equations by projecting the governing equations into the reduced space. However, the POD-Galerkin method requires access to the governing equations of the model, which may not be available in many cases. Therefore, significant work has been dedicated to mitigate this dependency by developing complete data-driven reduced modeling frameworks using artificial intelligence (e.g., Pawar et al. (2019); Wang et al. (2019)). Many of the methods developed rely on replacing the Galerkin projection step with a deep neural network that predicts the temporal evolution

of the coefficients associated with the POD modes. In light of this, various architectures have been used, including deep feedforward (e.g., Mjalled et al. (2023); Lui and Wolf (2019)), convolution (e.g., Wu et al. (2020)) and recurrent (e.g., Akbari et al. (2022)) neural networks, to name just a few.

Despite the advantage of POD as an effective tool to reduce the dimensionality of data, its linear basis approximation makes it incompatible with highly nonlinear systems where a large number of modes is required to capture the most dominant energy content of the data. Large numbers of modes are required because nonlinear phenomena are approximated as a linear combination of the POD modes. On the other hand, there are several available approaches to learning nonlinear manifolds, such as Kernel PCA (Zhou and Peng, 2020) and Laplacian eigenmaps (Belkin and Niyogi, 2003). These techniques, however, do not provide an analytical relationship to reconstruct the original data from the compressed representation. An alternative approach consists of using autoencoders (AEs) as a tool for learning nonlinear manifolds (e.g., Fu et al. (2023)). AEs not only offer the ability to learn intricate relationships within the data but also provide a structured means for reconstructing the high-dimensional representation.

AEs are a special type of unsupervised neural network that are trained to learn hidden features from an input. Their architecture consists of two parts, namely, the encoder and the decoder. The former compresses the high-dimensional input into a low-dimensional representation, while the latter learns how to reconstruct the input. AEs have been extensively used to build data-driven reduced models of flow fields around solid bodies. Fukami et al. (2021) investigated the ability of AEs for dimensionality reduction of flow field data in the wake of a two-dimensional cylinder. However, his work focused only on data compression and did not predict temporal evolution. In contrast, Xu and Duraisamy (2020) developed a multi-level AE reduced model that addresses all aspects of the flow, including dimensionality reduction, temporal evolution, and parameter variation. Hou et al. (2022) developed a hybrid AE-LSTM reduced model for the flow field prediction around submarines, where the LSTM (long short-term memory) layer has been utilized to resolve the dynamics of the compressed space. Hasegawa et al. (2020) proposed a method to construct AE-based reduced models for unsteady flows around bluff bodies of various shapes. Apart from AEs, other neural network architectures have been used to approximate flow fields around different shapes, such as airfoils (Sekar et al., 2019) and automobiles (Guo et al., 2016).

Different variations of AEs have been used for reduced flow field modeling. In their pioneering work, Pant et al. (2021) developed a reduced model framework based on 3D convolutional AE for the temporal evolution of fluid simulation. The model demonstrated accurate results across various simulations, including the flow field prediction around a 2D circular cylinder. In this work, we build upon their findings and extend the framework by making it parametric. This modification empowers the model to not only reproduce known simulations but also to predict the flow field corresponding to a new simulation parameter. We apply the extended framework to a bed configuration of hot particles, wherein we propose the usage of a post-processing non-trainable output layer to encompass the physical knowledge of the system into the prediction, e.g., no-slip condition at the fluid-solid interface.

The remainder of the paper is organized as follows. Sec. 2 presents the numerical model for generating the simulation database. A comprehensive overview of AEs is given in Sec. 3. Sec. 4 explains the framework used in this work to build a parametric data-driven reduced

model based on 3D convolutional AE. The results are presented and discussed in Sec. 5. Finally, conclusions are provided in Sec. 6.

2 Numerical model

We present in this section the governing equations together with a brief explanation of the numerical model used in this study. The model is validated by comparing the simulation results with benchmark data. The results of the numerical model will serve as training data for the reduced model.

2.1 Governing equations and lattice Boltzmann-finite difference model

A variation of the Navier-Stokes equations is employed that accounts for the compressibility arising from the variation of temperature. It should be noted that these equations hold true only in low Mach number flows. The governing equations that ensure the conservation of mass, momentum and energy for this model are:

$$\partial_t \rho + \nabla \cdot (\rho \mathbf{u}) = 0 \quad (1)$$

$$\partial_t (\rho \mathbf{u}) + \nabla \cdot (\rho \mathbf{u} \otimes \mathbf{u}) = -\nabla P_h + \nabla \cdot \boldsymbol{\tau} + \mathbf{F} \quad (2)$$

$$\partial_t \rho h + \nabla \cdot (\rho \mathbf{u} h) = -\nabla \cdot \mathbf{q} + \partial_t P_t \quad (3)$$

$$\rho = \frac{M_w P_t}{RT}, \quad (4)$$

where ρ , \mathbf{u} , $\boldsymbol{\tau}$ and \mathbf{F} represent the density, velocity, viscous stress tensor and body force per unit volume of the gas, respectively. Moreover, h , \mathbf{q} , R , M_w and T stand for enthalpy, heat flux, universal gas constant (as the gas is assumed ideal in our simulation), molecular weight and temperature of the gas, respectively. An important point to remark in this model is that pressure is divided into two parts, namely, hydrodynamic pressure (P_h) and thermodynamic pressure (P_t). P_h considers the spatial and temporal variation of the pressure within the flow. On the other side, P_t is uniform spatially and depends only on time.

To solve these equations, a combined lattice Boltzmann-finite difference (LB-FD) method was utilized. In particular, the lattice Boltzmann method was employed to model the flow field, which takes into consideration heat expansion, while the energy equation was solved using the finite difference method. The kinetic equations described below represent a modified version of the conventional lattice Boltzmann method that has the capability of recovering the thermal compressible form of Navier-Stokes equations beyond the Boussinesq approximation (see, e.g., Hosseini et al. (2019), for more details):

$$\frac{\partial g_\alpha}{\partial t} + \mathbf{c}_\alpha \cdot \nabla g_\alpha = -\frac{1}{\tau_r} (g_\alpha - g_\alpha^{\text{eq}}) + \Xi_\alpha, \quad (5)$$

$$\Xi_\alpha = (\mathbf{c}_\alpha - \mathbf{u}) \cdot [\nabla \rho c_s^2 (f^{\text{eq}}/\rho - w_\alpha) + f^{\text{eq}}/\rho] + \rho c_s^2 w_\alpha \nabla \cdot \mathbf{u}, \quad (6)$$

$$f_\alpha^{\text{eq}} = \rho w_\alpha \left(1 + \frac{1}{c_s^2} \mathbf{c}_\alpha \cdot \mathbf{u} + \frac{1}{2c_s^4} (\mathbf{c}_\alpha \cdot \mathbf{u})^2 - \frac{1}{2c_s^2} \mathbf{u}^2 \right), \quad (7)$$

$$g_\alpha^{\text{eq}} = c_s^2 f_\alpha^{\text{eq}} + w_\alpha (P_h - \rho c_s^2), \quad (8)$$

Table 1: Drag coefficient of square/circular body placed in a cross-flow at Reynolds number 100 under isothermal conditions. Δx is the distance between two adjacent grid points in both spatial directions.

	$\Delta x = 4 \times 10^{-4} \text{m}$	$\Delta x = 3 \times 10^{-4} \text{m}$	$\Delta x = 2 \times 10^{-4} \text{m}$	Benchmark data
square	1.556	1.549	1.548	1.43 (Sohankar et al., 1997)
circular	1.520	1.517	1.516	1.39 (Braza et al., 1986)

where g_α , \mathbf{c}_α , τ_r , w_α and f_α are the modified distribution function, discrete velocities, relaxation coefficient, weights, and the standard distribution function in the lattice Boltzmann model, respectively. Sutherland’s law is used to determine the dynamic viscosity μ , which is then used to compute the relaxation coefficients τ_r according to

$$\mu = \rho c_s^2 (\tau_r - 0.5). \quad (9)$$

The reader is referred to Namdar et al. (2023) for more details about the numerical model.

2.2 Validation of the numerical model

To ensure the validity of the numerical model, two tests were conducted and their corresponding results are compared against literature data. These tests involved simulating gas flow around a single 2D square or circular body at a Reynolds number of 100. Known velocity and pressure conditions were applied at inlet and outlet boundaries, respectively. The no-slip boundary condition was also applied on the fluid-solid contact while upper and lower boundaries were subjected to periodic boundary conditions. To evaluate the momentum exchange, the drag coefficient C_D was calculated for the isothermal case employing different grid resolutions. We present the obtained results in Tab. 1 and compare them to benchmark data. The results demonstrate the convergence of the mesh starting from $\Delta x = 3 \times 10^{-4} \text{m}$, and an agreement with the benchmark data is obtained within a tolerable deviation of 9%.

To validate the heat transfer rate, a similar analysis is performed to compute the Nusselt number Nu for a flow passing over square/circular body with 100K temperature difference. The calculation of the local Nu and average \overline{Nu} is according to the definitions given by Vierendeels et al. (2003):

$$Nu = \frac{D}{\lambda_0 (T_{\text{particle}} - T_{\text{inlet}})} \left(\lambda \frac{\partial T}{\partial n} \right)_{\text{surf}}, \quad (10)$$

$$\overline{Nu} = \frac{1}{A} \int_A Nu dA, \quad (11)$$

where λ and λ_0 are the heat conductivity of gas evaluated at temperature of the particle surface and mean temperature $T_0 = (T_{\text{particle}} + T_{\text{inlet}})/2$, respectively. As the Prandtl number

Table 2: Average Nusselt numbers of square/circular body placed in a cross-flow at Reynolds number 100. The temperatures of gas and solid bodies are 300K and 400K, respectively.

	$\Delta x = 4 \times 10^{-4} \text{m}$	$\Delta x = 3 \times 10^{-4} \text{m}$	$\Delta x = 2 \times 10^{-4} \text{m}$	Benchmark data
square	4.217	4.136	4.135	4.03 (Sharma and Eswaran, 2004)
circular	5.365	5.314	5.311	5.23 (Sharma and Eswaran, 2004)

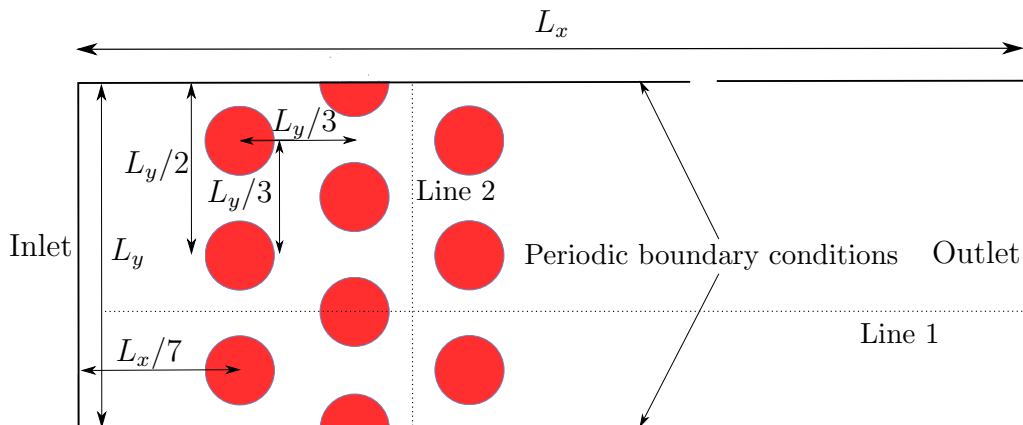


Figure 1: Schematic representation of the 2D computational domain used to model the flow field and heat exchange in a bed configuration of hot particles. The dotted lines, denoted as Line 1 and Line 2, serve as demonstration lines for evaluating our model in Sec. 5.

Pr is assumed to be constant, the heat conductivity is computed as $\lambda = (\mu c_p)/Pr$. The results depicted in Tab. 2 show an agreement between the obtained \overline{Nu} and the benchmark results within an accuracy of 2%.

Based on the results reported in Tabs. 1 and 2 for the flow around single particle, the validity of the solver is approved.

2.3 Simulation setup

The setup of the simulation is shown in Fig. 1. The spatial dimension is 2D, wherein three rows of circular particles are arranged at a specific distance from each other. The numerical domain is discretized using a cartesian grid of size 1800×350 . The corresponding simulation parameters are depicted in Tab. 3. This simple configuration is chosen in a first step to investigate the ability of deep learning to build reduced models for flow fields in packed bed configurations. Despite the relatively sparse arrangement of particles, the implementation of periodic boundary conditions at the side boundaries of the bed helps to minimize surface effects and thus mimic bulk behavior to a certain degree.

Table 3: Parameters used to perform the simulations shown in Fig. 1.

Parameter	Value	Parameter	Value
Fluid phase	Air	Solid phase	Aluminium
Time step (s)	6.2×10^{-7}	Diameter (m)	3.0×10^{-3}
Grid size (m)	4.3×10^{-5}	T_{particle} (K)	300 - 1200
Lx (m)	7.74×10^{-2}	T_{inlet} (K)	300
Ly (m)	1.5×10^{-2}	$P_{\text{t,inlet}}$ (Pa)	1.0×10^5
$c_{p,\text{air}}$ ($\text{J kg}^{-1} \text{K}^{-1}$)	1.0×10^3	$M_{w,\text{air}}$ (kg mol^{-1})	2.9×10^{-2}
Re	200	Pr	0.71

3 A brief introduction to autoencoders

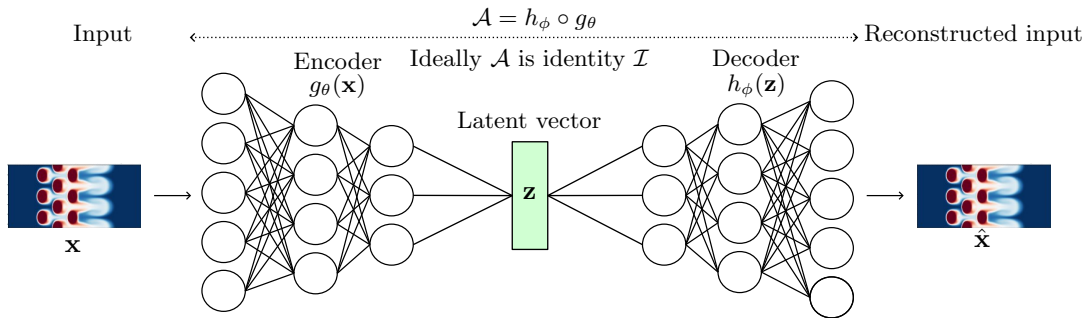


Figure 2: Example representation for a fully-connected autoencoder.

AEs were first introduced by Rumelhart et al. (1986a) as neural networks trained to reproduce their inputs. Unlike supervised learning, which relies on input-output pairs with explicit labels, training AEs is considered unsupervised learning because it does not require labeled data to be trained. Their objective is to learn an identity mapping \mathcal{A} . In general, \mathcal{A} can be identified using a neural network composed of two sub-networks, an encoder and a decoder. The encoder function $g_{\theta}(\mathbf{x}) : \mathbb{R}^N \rightarrow \mathbb{R}^p$ maps the input \mathbf{x} into a lower dimensional representation \mathbf{z} , referred to as the latent vector, such that $p \ll N$. The latent vector \mathbf{z} is then passed to the decoder function $h_{\phi}(\mathbf{z}) : \mathbb{R}^p \rightarrow \mathbb{R}^N$ which generates an approximated solution $\hat{\mathbf{x}}$ to the input. The indices θ and ϕ refer to the training parameters of the encoder and decoder networks, respectively. Training an AE consists of finding the optimal training parameters θ and ϕ that minimize a loss function $\mathcal{L}(\mathbf{x}, \hat{\mathbf{x}})$ between the original and reconstructed inputs, i.e.,

$$\theta_{\text{opt}}, \phi_{\text{opt}} = \operatorname{argmin}_{\theta, \phi} \mathcal{L}(\mathbf{x}, h_{\phi}(g_{\theta}(\mathbf{x}))). \quad (12)$$

By capturing the most important features and patterns of the input, the AE compresses the input into a condensed representation through its encoder function. This compression technique involves reducing the dimensionality of the input while maintaining critical information. In this sense, AEs can be considered as a nonlinear generalization of POD.

The AE architecture can be varied depending on the data type and its input format. Several types of AEs have been developed (Zhai et al., 2018), each tailored to address specific problems or exploit particular data features. In this paper, we will provide an overview of those relevant to our work.

3.1 Fully-connected autoencoder

This variant of AE uses fully-connected layers to find a compressed representation \mathbf{z} for the input \mathbf{x} (see Fig. 2). Every fully connected layer performs the following operation:

$$\mathbf{y} = \mathbf{f}(\mathbf{W}\mathbf{x} + \mathbf{b}), \quad (13)$$

where $\mathbf{y} \in \mathbb{R}^l$ is the output of the layer (input of the following layer in a deep network), $\mathbf{W} \in \mathbb{R}^{l \times N}$ is a weight matrix and $\mathbf{b} \in \mathbb{R}^l$ is the bias vector. The nonlinear activation function $\mathbf{f} : \mathbb{R}^l \rightarrow \mathbb{R}^l$ is applied element-wise to the output of the affine transformation. This variation of AE is not suitable for handling high-resolution 2D input images due to its requirement of flattening the input into a 1D vector. In addition, flattening the image results in disregarding the spatial structure, i.e., the spatial connections between neighboring pixels are not explicitly maintained. An alternative would be to use convolutional layers to preserve the spatial information.

3.2 Convolutional autoencoder

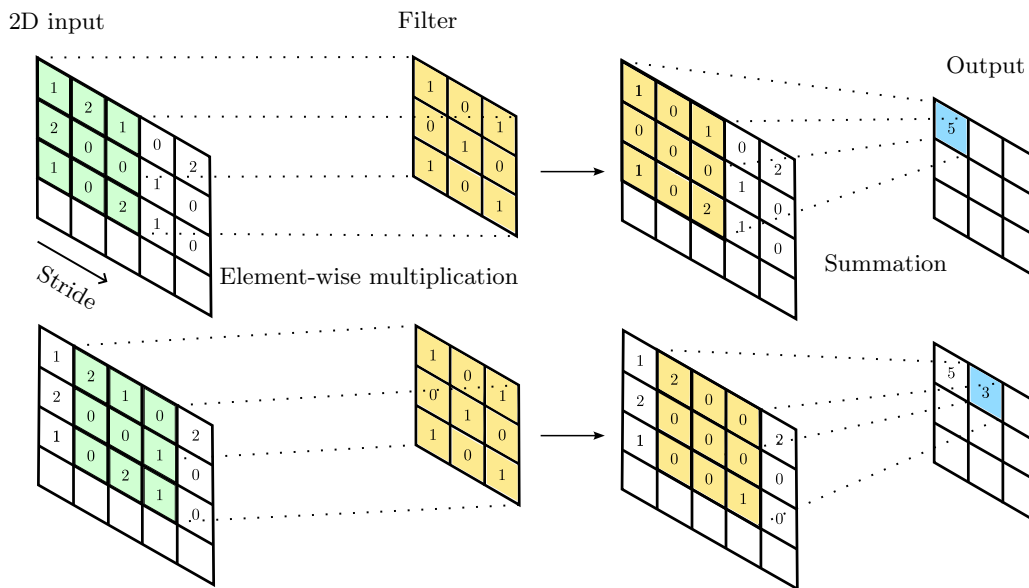


Figure 3: 2D convolution operation with a 3×3 filter and stride 1. Element-wise multiplication takes place between the filter and the corresponding entries of the input. The results are summed to calculate the output, followed by applying a nonlinear activation function in the way described in (13).

In this variation of AE, the fully connected layers are replaced by convolutional layers. They are frequently used in computer vision tasks because they capture spatial dependencies effectively (see, e.g., Geng and Song (2016)). As the name suggests, a convolutional layer applies a convolution operation to its input. Convolution is the process of applying a kernel or filter to the input data and computing the element-wise multiplications between the filter entries and the corresponding input values. The results are then summed. Mathematically, the convolutional operation is expressed in the same way presented in (13) with \mathbf{W} being a circular matrix. An illustration of a 2D convolutional operation is shown in Fig. 3. It should be noted that the underlying convolutional principle is the same for 1D and 3D cases.

3.3 Temporal autoencoder

Temporal AEs are used in many applications, e.g., video prediction and motion forecasting, where temporal coherence needs to be learned from sequential data (see, e.g., Zhao et al. (2017)). The working principle of a temporal AE is slightly different from that of the conventional one described above. In a temporal AE, the focus is on the prediction of the temporal evolution of the input data, i.e.,

$$\mathbf{x}(t+1) = \mathcal{T}(\mathbf{x}(t)), \quad (14)$$

where $\mathbf{x}(t)$ and $\mathbf{x}(t+1)$ denote the input variable at the current and next timesteps, respectively, and \mathcal{T} is the neural network that encloses the encoder and decoder functions. Temporal AEs require supervised learning because the temporal dependency is learned by providing the ground truth sequence during training. Both fully-connected and convolutional layers can be used to build the architecture of the temporal AE. The terminology autoencoder is used here to describe the underlying structure of an encoder-decoder model. Its use, however, departs from the conventional approach defined earlier, where the encoder compresses the input data, and the decoder reconstructs it at the output layer. Instead, in a temporal AE, the encoder learns temporal relationships from a sequence, and the decoder reconstructs the data which serves as input at the following timestep (see Fig. 4).

4 Data-driven reduced model

We extend the framework introduced by Pant et al. (2021) for constructing a neural network-based reduced model for fluid simulations by making it parametric, i.e., the dynamics are predicted for new values of the parameters that were not used during training. The reduced model is represented as a 3D temporal convolutional AE.

4.1 Model architecture

We define the snapshot $\mathbf{s}(t_m) \in \mathbb{R}^{N_x \times N_y \times N_v}$ as a multichannel image of the flow field solution at time step t_m . Each of the N_v channels represents the solution of a flow field variable (velocity magnitude or temperature in our case) defined on a uniform 2D Cartesian grid of dimension $N_x \times N_y$.

Dynamic flow field simulations can be analyzed by temporal sequence of solution snapshots. Given the previous h snapshots and the corresponding simulation parameter value μ ,

the reduced model predicts the flow field solution at the next time step, i.e.,

$$\mathbf{s}(t_{h+1}) \approx \mathcal{N}(\mu, \mathbf{s}(t_0), \dots, \mathbf{s}(t_h)), \quad (15)$$

where \mathcal{N} is a nonlinear function that results from training a 3D temporal convolutional AE. As an extension of the 2D convolutional layers illustrated in Sec. 3.2, the 3D convolutional layer used here not only operate on the spatial but also on the temporal dimension. Therefore, they are well suited for applications where both the spatial and temporal dimensions of the data are significant, such as video classification, action recognition, and spatio-temporal segmentation. The parametric data-driven reduced model framework and the model architecture are presented in Fig. 4. The 3D temporal convolutional AE used in this work employs an encoding-decoding path to learn the underlying dynamics of the spatio-temporal data. The encoding path consists of four 3D convolutional layers with a tanh activation function. A connection of non-trainable layers precedes the encoding path of our model to combine the different inputs to the model, i.e., the input sequence and the corresponding simulation parameter μ , which is the temperature of the solid particles in our simulation. It should be noted that μ is given to the network as an image of the initial condition of the flow. The image format of the parameter value facilitates the combination of μ with the other inputs, as they are also presented in image form. Once the temporal sequence has been analyzed in the encoding path, the neural network predicts the solution at the next time step by reconstructing the flow field image with the original size in the decoding path. For this purpose, four 2D convolutional transpose layers with tanh activation are used. The decoding path is followed by a non-trainable post-processing layer that effectively utilizes the physical information embedded within the parameter image. Specifically, we use the location of particles to enforce a no-slip condition to guide the prediction. Incorporating these constraints will improve the prediction accuracy of our framework. In order to improve the efficiency of the training, we use a batch normalization layer after every intermediate convolutional operation. This technique helps to speed up convergence and reduce overfitting (Ioffe and Szegedy, 2015). Tab. 4 shows the detailed architecture of the model. In this architecture, all the convolutional layers operate with a stride of 2 in all image dimensions to systematically decrease/increase the output size. The filter size used for the 3D convolutional layers is $2 \times 4 \times 4$, while the 2D convolutional transpose layers use a filter of size 4×4 .

4.2 Input and output datasets

The training data used in this study comprises high-dimensional simulation snapshots $\mathbf{s}(t_m)$ and their corresponding simulation parameter μ . The high-dimensional snapshots are obtained from solving the numerical model described in Sec. 2, and to make them compatible with the input layer of the neural network, they are first interpolated on a uniform Cartesian grid of dimension 256×128 . The interpolated values are considered ground truth and will be used to train and evaluate our model. Subsequently, the interpolated snapshots are normalized between -1 and 1 for numerical stability during the training process according to

$$\chi_{\text{norm}} = 2 \cdot \frac{\chi - \chi_{\min}}{\chi_{\max} - \chi_{\min}} - 1, \quad (16)$$

where χ is the corresponding pixel value of the image and χ_{\min} and χ_{\max} are the minimum and maximum pixel values, respectively, identified for all snapshots for all training simulations

Table 4: Detailed architecture of the 3D convolutional autoencoder. All convolutional and transpose convolutional layers use a stride of 2 in all image dimensions. The dimensions shown in this table correspond to $h = 10$ and $N_x \times N_y = 256 \times 128$.

Layer	Output Shape	Corresponding input(s)
Pre-processing		
ParameterImage (Input)	(None, 256, 128)	[]
ExpandLayer1	(None, 256, 128, 1)	[ParameterImage]
ExpandLayer2	(None, 1, 256, 128, 1)	[ExpandLayer]
SequenceImages (Input)	(None, 10, 256, 128, 2)	[]
Tile	(None, 10, 256, 128, 1)	[ExpandLayer2]
Concatenate	(None, 10, 256, 128, 3)	[SequenceImages, Tile]
Encoding path		
Conv3D-1	(None, 5, 128, 64, 64)	[Concatenate]
Conv3D-2	(None, 3, 64, 32, 128)	[Conv3D-1]
BatchNorm-1	(None, 3, 64, 32, 128)	[Conv3D-2]
Conv3D-3	(None, 2, 32, 16, 256)	[BatchNorm-1]
BatchNorm-2	(None, 2, 32, 16, 256)	[Conv3D-3]
Conv3D-4	(None, 1, 16, 8, 512)	[BatchNorm-2]
BatchNorm-3	(None, 1, 16, 8, 512)	[Conv3D-4]
Reshape	(None, 16, 8, 512)	[BatchNorm-3]
Decoding path		
Conv2D-transpose-1	(None, 32, 16, 256)	[Reshape]
BatchNorm-4	(None, 32, 16, 256)	[Conv2D-transpose-1]
Conv2D-transpose-2	(None, 64, 32, 128)	[BatchNorm-4]
BatchNorm-5	(None, 64, 32, 128)	[Conv2D-transpose-2]
Conv2D-transpose-3	(None, 128, 64, 64)	[BatchNorm-5]
BatchNorm-6	(None, 128, 64, 64)	[Conv2D-transpose-3]
Conv2D-transpose-4	(None, 256, 128, 2)	[BatchNorm-6]
Post-processing		
Output	(None, 256, 128, 2)	[ParameterImage, Conv2D-transpose-4]

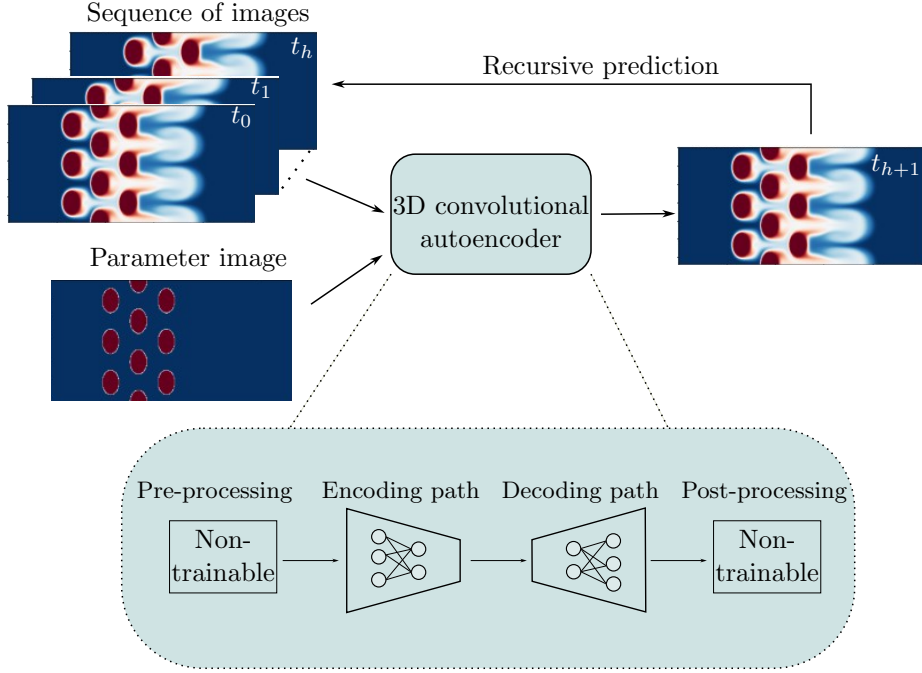


Figure 4: Data-driven framework for the parametric prediction of flow field simulations in packed bed configuration using 3D convolutional autoencoder.

parameterized with μ . It is important to note that each image channel, i.e., variable field, is scaled separately. The parameter images are also normalized as they are considered another input to the neural network.

For the purpose of training, the snapshots are structured sequentially:

$$X(\mu) = \begin{bmatrix} \mathbf{s}(t_0) & \mathbf{s}(t_1) & \cdots & \mathbf{s}(t_h) \\ \mathbf{s}(t_1) & \mathbf{s}(t_2) & \cdots & \mathbf{s}(t_{h+1}) \\ \vdots & \vdots & \cdots & \vdots \\ \mathbf{s}(t_{N_t-h-1}) & \mathbf{s}(t_{N_t-h}) & \cdots & \mathbf{s}(t_{N_t-1}) \end{bmatrix}, \quad Y(\mu) = \begin{bmatrix} \mathbf{s}(t_{h+1}) \\ \mathbf{s}(t_{h+2}) \\ \vdots \\ \mathbf{s}(t_{N_t}) \end{bmatrix}, \quad (17)$$

where N_t is the total number of simulation snapshots, X is the sequence of images given as input and Y is the corresponding output for a single simulation.

4.3 Offline training and online prediction

The supervised learning approach is used to approximate \mathcal{N} , which consists of finding the optimal training parameters θ that minimizes a loss function $\mathcal{L}(\mathbf{s}(t_m), \hat{\mathbf{s}}(t_m))$ between the ground truth $\mathbf{s}(t_m)$ and the predicted solution $\hat{\mathbf{s}}(t_m)$

$$\theta_{\text{opt}} = \operatorname{argmin}_{\theta} \mathcal{L}(\mathbf{s}(t_m), \hat{\mathbf{s}}(t_m)). \quad (18)$$

The optimization problem shown in (18) can be solved using the gradient descent algorithm or one of its variants, such as the Adam optimizer (Kingma and Ba, 2014). Backpropagation

Algorithm 1 Offline training

Require: $\{\mu^1, \dots, \mu^{N_s}\}$, Epochs, learning rate = l_r ;

```
1: for  $s = 1, \dots, N_s$  do
2:   Build  $X(\mu^s)$  and  $Y(\mu^s)$ ;
3:   Add to the complete training inputs array  $X \leftarrow X(\mu^s)$ ;
4:   Add to the complete training outputs array  $Y \leftarrow Y(\mu^s)$ ;
5:   Add to the parameter array  $\mu \leftarrow Y(\mu^s)$ ;
6: end for
7: Initialize the trainable parameters  $\theta$  randomly;
8: for  $i = 1, \dots$ , Epochs do
9:   for  $j = 1, \dots$ , length( $X$ ) do
10:    Feedforward in the network to make a prediction  $\hat{\mathbf{s}} = \mathcal{N}(\mu[j], X[j])$ ;
11:    Compute the loss  $\mathcal{L}(Y[j], \hat{\mathbf{s}})$ ;
12:    Compute the partial derivatives  $\frac{\partial \mathcal{L}}{\partial \theta}$ ;
13:    Update the trainable parameters using gradient descent algorithm  $\theta \leftarrow \theta - l_r \frac{\partial \mathcal{L}}{\partial \theta}$ ;
14:   end for
15: end for
16: return  $\mathcal{N}$ 
```

(Rumelhart et al., 1986b) is used to compute the partial derivatives required to update the trainable parameters θ . The optimization process continues until convergence or until a certain stopping criterion is met. The training procedure is summarized in Algorithm 1.

Algorithm 2 Online prediction

Require: $\mathcal{N}, \mu^{\text{val}}, h, \chi_{\min}, \chi_{\max}$;

```
1: for  $m = 0, \dots, h$  do
2:   Solve the numerical model for  $\mathbf{s}(t_m)$ ;
3:   Scale the snapshot using (16);
4: end for
5: for  $m = h, \dots, N_t - 1$  do
6:   make a prediction  $\mathbf{s}(t_{m+1}) = \mathcal{N}(\mu^{\text{val}}, \mathbf{s}(t_m), \dots, \mathbf{s}(t_{m-h}))$ ;
7:   Unscale the prediction  $\mathbf{s}^{\text{orig}}(t_{m+1}) = \frac{1}{2}(\mathbf{s}(t_{m+1}) + \mathbf{1})(\chi_{\max} - \chi_{\min}) + \chi_{\min}$ ;
8:   Add to the prediction array  $\mathbf{S}^{\text{orig}} \leftarrow \mathbf{s}^{\text{orig}}(t_{m+1})$ ;
9: end for
10: return  $\mathbf{S}^{\text{orig}}$ 
```

Once the neural network has been trained, it can be used to predict the flow field solution for a new value of μ that was not used during training. The prediction process starts by providing the first h snapshots as an input to the model. In this work, we use the ground truth snapshots to make our initial predictions. We emphasize that the prediction is recursive (see Fig. 4). The online step is concluded with an unscaling process to revert the snapshots to their original scale. Algorithm 2 summarizes the prediction of the flow field solution given a new value of the simulation parameter.

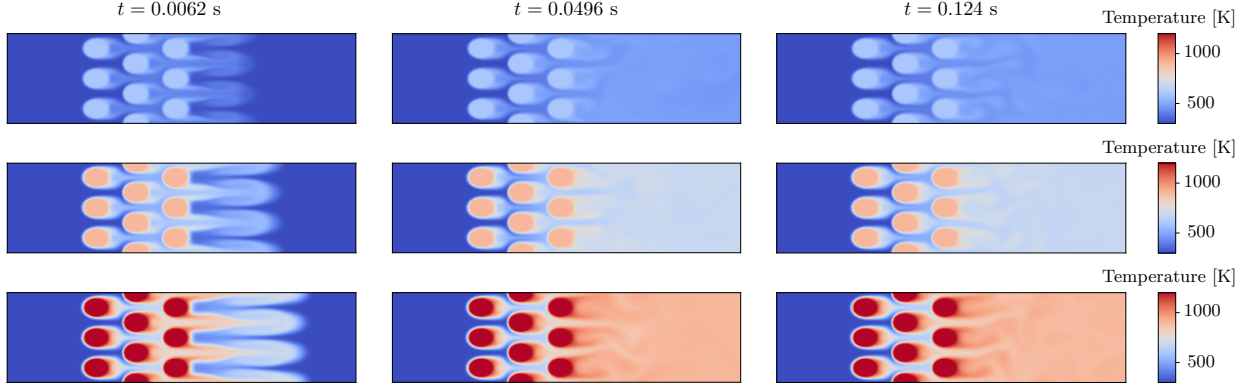


Figure 5: A comparison of temperature fields in snapshots obtained from simulations parametrized with (top) $T^{\text{par, tr}} = 600$ K, (middle) $T^{\text{par, tr}} = 900$ K, and (bottom) $T^{\text{par, tr}} = 1200$ K. The snapshots correspond to time steps $t = 0.0062, 0.0496, 0.124$ s.

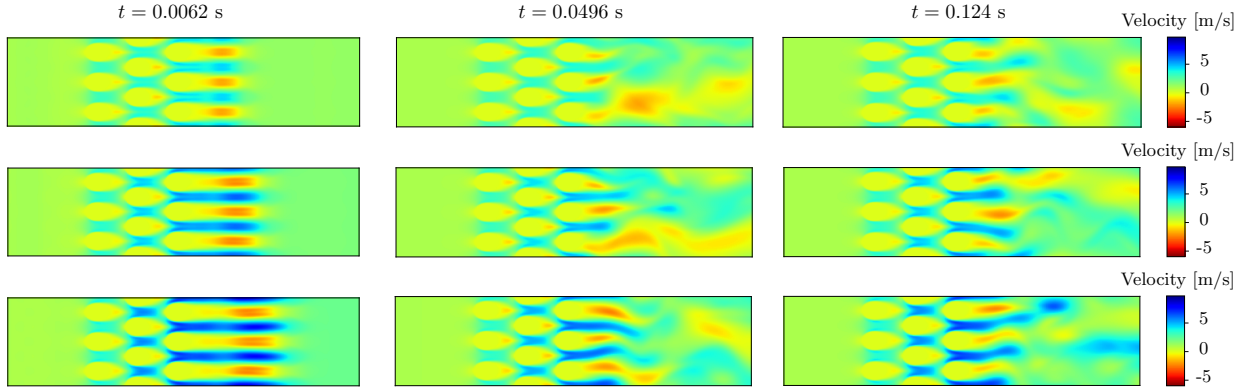


Figure 6: A comparison of velocity fields in snapshots obtained from simulations parametrized with (top) $T^{\text{par, tr}} = 600$ K, (middle) $T^{\text{par, tr}} = 900$ K, and (bottom) $T^{\text{par, tr}} = 1200$ K. The snapshots correspond to time steps $t = 0.0062, 0.0496, 0.124$ s.

5 Results

We present a comprehensive evaluation of the performance of the parametric 3D temporal convolutional AE in this section. Our primary objective is to develop a data-driven framework for the high-dimensional dynamic system presented in Sec. 2. The neural network consists of the 3D temporal convolutional AE explained in Sec. 4 that predicts the flow field solution at the next timestep given the previous $h = 10$ snapshots and the corresponding value of μ . The length h of the input sequence is a hyperparameter of the model and can be adjusted if needed.

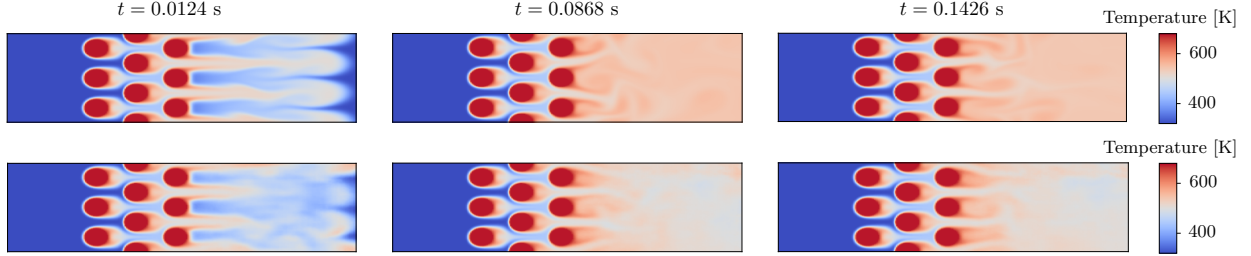


Figure 7: Comparison of the temperature fields obtained from (top) lattice Boltzmann method and (bottom) 3D convolutional autoencoder at time levels $t = 0.0124, 0.0868, 0.1426$ s. The results correspond to a validation simulation parameterized with $T^{\text{par, val}} = 750$ K.

5.1 Comparative analysis between the high-fidelity and the reduced models

The training and validation datasets were obtained by running the high-fidelity model presented in Sec. 2. Each simulation is parameterized by the temperature of the particles T^{par} . The neural network is trained using Algorithm 1 for the particle temperature parameters $T^{\text{par, tr}} = 300, 400, 500, 600, 700, 800, 900, 1000, 1100, 1200$ K. A total number of 4000 snapshots (400 for every training simulation) were collected with a uniform timestep of 6.2×10^{-4} s. Figures 5 and 6 provide a representative comparison of snapshots obtained from different training simulations, showcasing the temperature and velocity fields, respectively. In the context of temperature fields in Fig. 5, the increase in particle temperatures is associated with more heat transfer between particles and the fluid medium. Notably, consistent patterns in the transient solution can be observed across various simulations, albeit with varying amplitudes corresponding to particle temperatures. This trend is also observed in the post-transient solution, with minimal variation among different simulations in the wake behind the cylinders of the last row. On the other hand, the velocity field results presented in Fig. 6 show that the solution structure is similar only during the transient phase, while the post-transient solution exhibits large structural variation between various simulations, particularly in the downstream region. In addition, across all training simulations, it is observed that the velocity field does not converge to a limit cycle.

In the training phase of the reduced model, we employ the Adam optimizer (Kingma and Ba, 2014) with a learning rate of $\eta = 0.001$ and a batch size of $N_b = 10$ to find the optimal training parameters θ_{opt} . The loss function used is the mean squared error, and the neural network is trained for 250 epochs using the open-source deep learning library TensorFlow (Abadi, 2016). Once the model is trained, we use Algorithm 2 to predict the flow field solution for a new value of μ . Figures 7 and 8 evaluate the parametric 3D convolutional autoencoder model for the validation parameter $T^{\text{par, val}} = 750$ K. The snapshots shown are chosen randomly and correspond to the solutions at $t = 0.0124, 0.0868, 0.1426$ s for the temperature field (Fig. 7) and velocity field (Fig. 8). It is evident that the first half of the domain, i.e., the interstitial flow between particles, was accurately predicted by our model with a very small visual difference in both temperature and velocity fields. However, as we

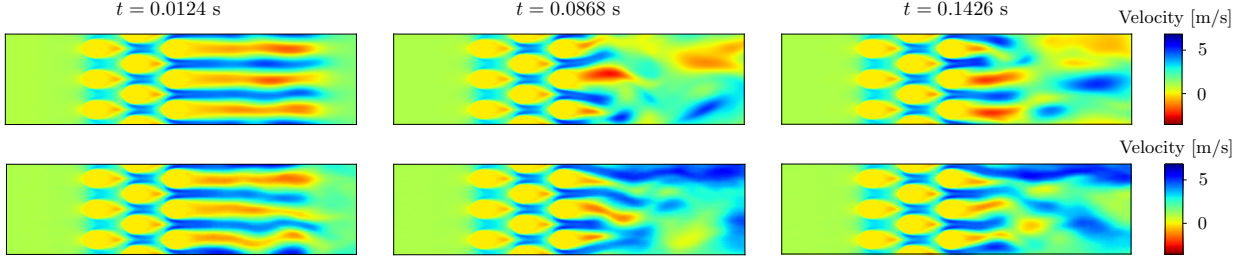


Figure 8: Comparison of the magnitude of the velocity fields obtained from (top) lattice Boltzmann method and (bottom) 3D convolutional autoencoder at time levels $t = 0.0124, 0.0868, 0.1426$ s. The results correspond to a validation simulation parameterized with $T^{\text{par, val}} = 750$ K.

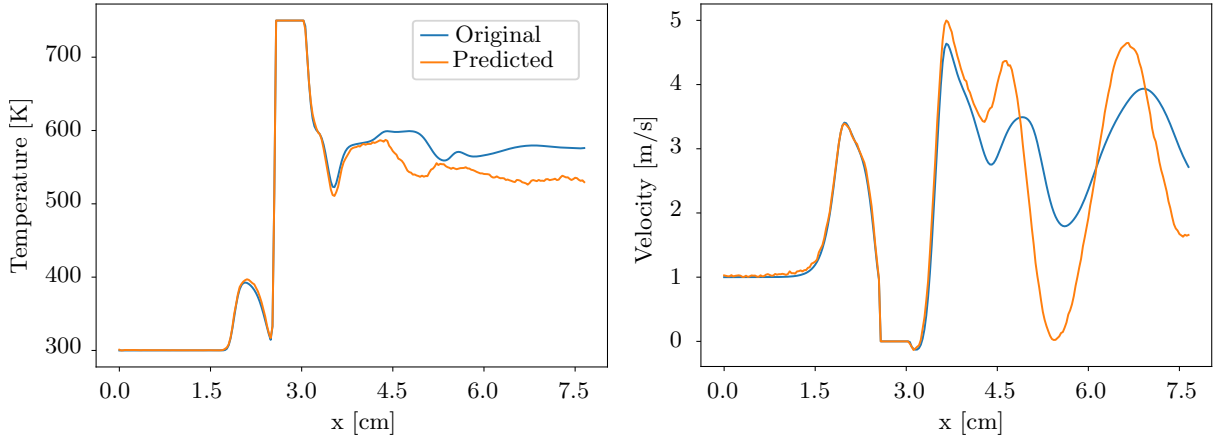


Figure 9: Comparison between (blue) original and (orange) predicted solutions for the temperature and velocity along Line 1, illustrated in Fig. 1, at time $t = 0.1426$ s. The results correspond to a validation simulation parameterized with $T^{\text{par, val}} = 750$ K.

move downstream, a decline in the prediction accuracy becomes more visible in the temperature field, and to a greater extent in the velocity field. Specifically, only the overall vortex shedding pattern is predicted in the downstream region without matching the spatial details. These findings reflect the properties of the available training dataset and the differences highlighted in Figs. 5 and 6, where the effect of parameter variation on the temperature field is well represented by the training simulations, but less effectively conveyed in the velocity field within the downstream region.

For the sake of a more quantitative comparison, the variations of the temperature and velocity along Line 1 and Line 2 from Fig. 1 are plotted in Figs. 9 and 10. These plots, generated at randomly chosen time steps, correspond to two validation simulations parameterized with $T^{\text{par, val}} = 550$ K and $T^{\text{par, val}} = 750$ K. Results demonstrate the capability of the parametric 3D convolutional AE to predict the flow field solution in a bed configuration of particles. However, a noticeable deviation from the original solution is evident in the downstream domain where the flow becomes chaotic. This deviation is attributed to the

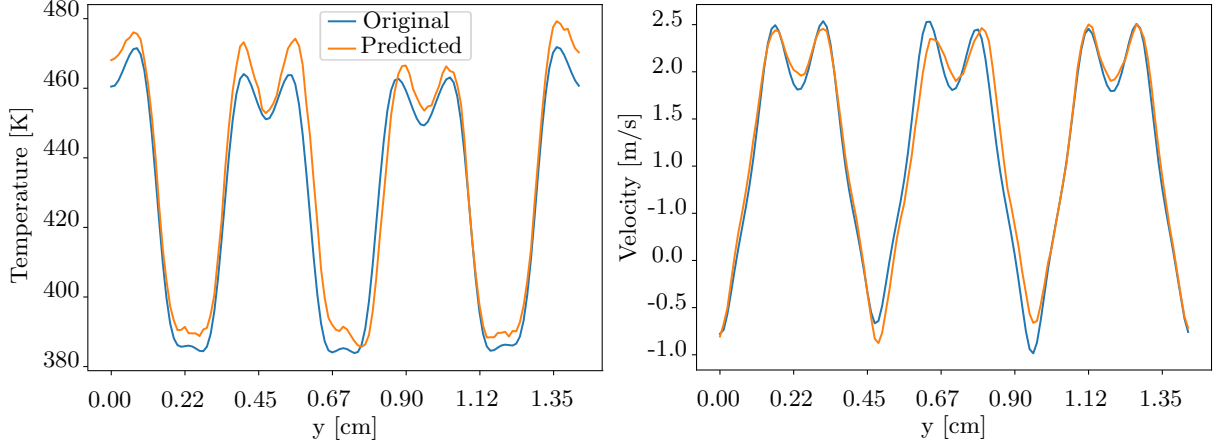


Figure 10: Comparison between (blue) original and (orange) predicted solutions for temperature and velocity along Line 2, illustrated in Fig. 1, at time $t = 0.093$ s. The results correspond to a validation simulation parameterized with $T^{\text{par, val}} = 550$ K.

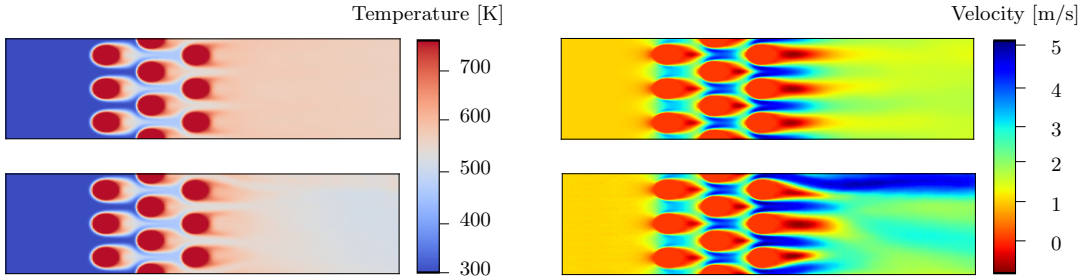


Figure 11: Temporal average fields obtained from (top) lattice Boltzmann method and (bottom) 3D convolutional autoencoder for the simulation parameterized with $T^{\text{par, val}} = 750$ K.

limited number of training simulations and the recursive prediction property of the model, which render accurate flow field prediction in chaotic regions a highly challenging task. It is important to emphasize, however, that the model sufficiently captures the main flow pattern of vortex shedding, which is the dominant flow behavior in this region.

5.2 Structural Comparison using proper orthogonal decomposition

We pursue our evaluation of the reduced model by comparing the full original and predicted simulations for the validation parameter $T^{\text{par, val}} = 750$ K. For this purpose, we employ POD (see Appendix. A for a brief introduction to POD) as a means to extract and compare the dominant structures in the temperature and velocity fields of both results. In the beginning, we decompose the quantities of interest into mean and fluctuation parts. The corresponding temporal average fields are shown in Fig. 11. A good agreement is observed between the averages obtained from the lattice Boltzmann method and the 3D convolutional autoencoder

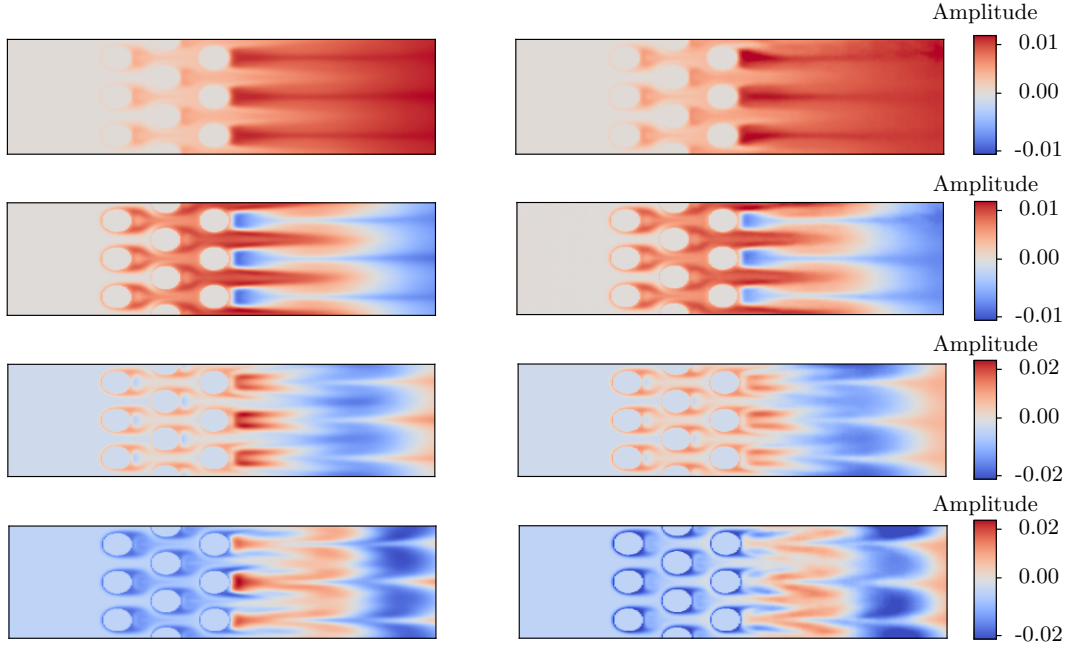


Figure 12: The four most dominant temperature modes, arranged from top to bottom. The left column corresponds to simulation results obtained from the lattice Boltzmann method, and the right column corresponds to results predicted using the 3D convolutional autoencoder for the simulation parametrized with $T^{\text{par, val}} = 750$ K.

in the temperature field. However, the predicted velocity in the downstream region is, on average, higher than the original one. Remarkably, the greatest difference is located near to the upper boundary, where a high-velocity stream is predicted. The four most dominant POD temperature modes of the predicted simulation are compared with the original ones in Fig. 12. The results demonstrate strong agreement between the two sets of modes, with a slight discrepancy appearing in higher modes. Subsequently, we illustrate in Fig. 13 the power spectra for the temporal coefficients associated with each of the POD temperature modes presented. It should be noted that a one-to-one comparison is only meaningful in our case due to the highly similar structure of the POD temperature subspaces. The comparison of spectra reveals a notable agreement in the high-frequency domain, suggesting consistent short-term dynamics across both the original and predicted simulations. However, the congruent patterns in the low-frequency region point to slightly different long-term dynamics. Additionally, it is observed that the two spectra deviate as we progress to higher modes.

Similarly, we apply the POD method to the velocity field. The four most dominant POD velocity modes are compared in Fig. 14. The results show that the near-upper-wall velocity stream, depicted in the mean of the predicted simulation in Fig. 11, is only partially visible in the first original POD velocity mode. Upon a direct comparison of the modes, it becomes evident that both simulations exhibit the vortex shedding pattern in the downstream region, although with differing structures. Specifically, the dominant pattern in the predicted solution consists of small-scale vortices, while the real solution features slightly larger ones. For completeness, we illustrate in Fig. 15 the spectra of the temporal coefficients associated

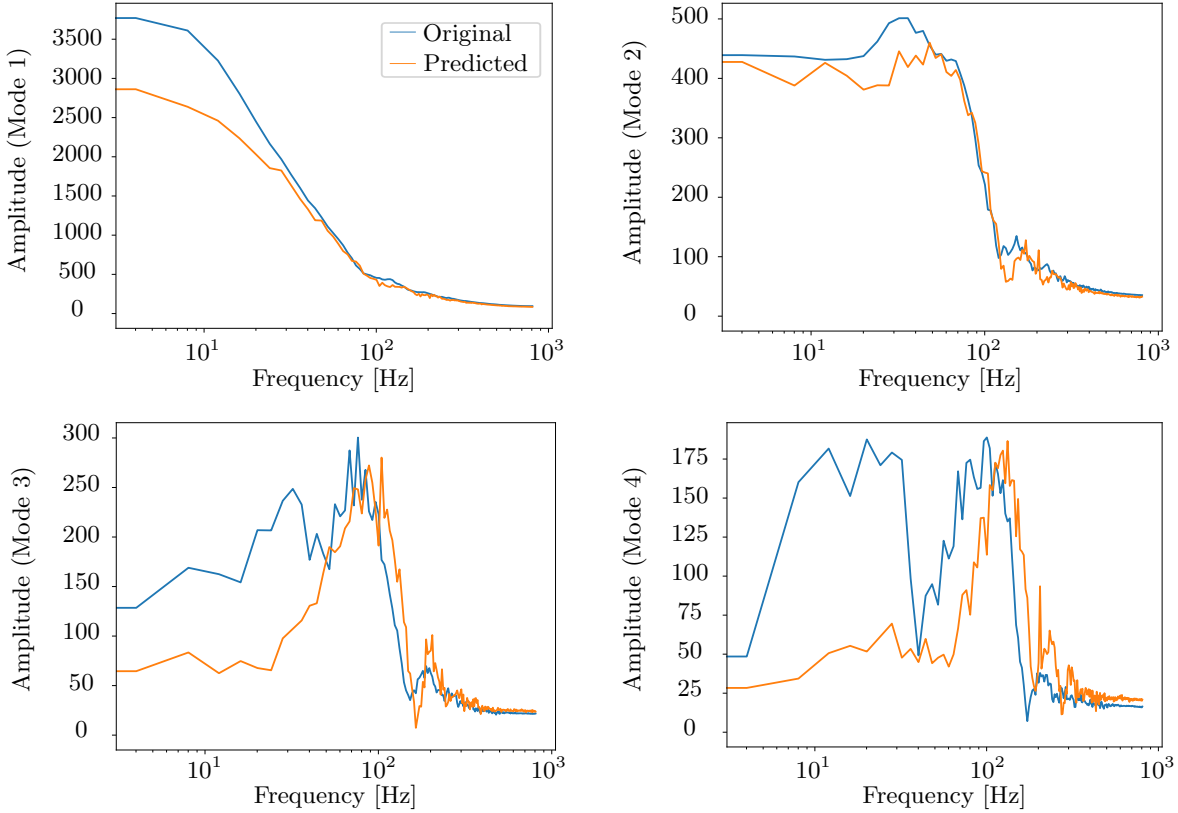


Figure 13: Power spectra for the temporal coefficients associated with the four most dominant POD temperature modes.

with the shown POD velocity modes. However, a direct comparison is not feasible due to the distinct structure of the underlying POD subspaces.

In our case, the primary focus lies in predicting the transient and the post-transient solutions in the interstitial flow region between particles. The downstream domain may not always require precise prediction in many practical applications. Instead, we can highlight the model’s ability to accurately predict the flow field solution in the void space between particles in a bed configuration. Figures 7 to 15 show that our reduced model can predict the flow field solution for new simulation parameters well and that the dominant prediction errors are mainly located in the highly downstream region.

5.3 Comparison of the computational time

While providing a precise comparison of the computational time required to evaluate the high-dimensional model against the reduced model is not possible due to the fine grid (1800×350) used for the numerical solution, we directly compare the average computational time required to solve the high fidelity simulation ¹ (≈ 27365 s) to that of the evaluation of the reduced

¹The high-fidelity model was solved on an Intel Xeon W-2255 CPU @ 3.7GHz 20

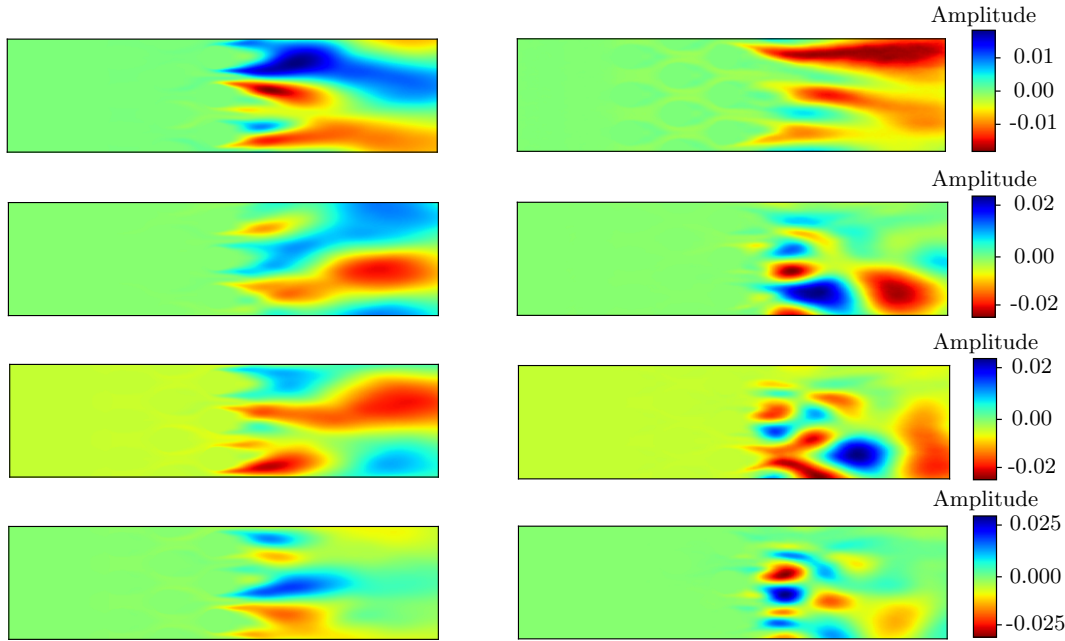


Figure 14: The four most dominant velocity modes, arranged from top to bottom. The left column corresponds to simulation results obtained from the lattice Boltzmann method, and the right column corresponds to results predicted using the 3D convolutional autoencoder for the simulation parametrized with $T^{\text{par, val}} = 750$ K.

model ² (≈ 63 s). It is evident that a significant reduction in the computational time is obtained.

6 Conclusion

In this work, a reduced model for predicting flow fields in a bed configuration of hot spheres has been developed. The model is data-driven and does not require access to the governing equations of the high-fidelity model. Our work builds upon a previous study by Pant et al. (2021), who use a 3D temporal convolutional autoencoder to learn a temporal sequence of 2D flow field snapshots to predict the temporal evolution. In our study, we have extended this framework by making it parametric, allowing the model to predict the solution for an unseen value of the parameter. Therefore, our reduced model learns reduced order embeddings of high-dimensional dynamic systems and substantially reduces the computational time required to approximate the solution for a new value of the parameter. Moreover, the framework presented here suggests using a post-processing non-trainable output layer to incorporate the available physical knowledge of the system into the prediction. This is helpful to improve the overall quality of the results because the output of the model is stacked with the inputs at the next time step.

In order to evaluate our model, we compared the original results of a simulation param-

²The reduced model was trained and evaluated on an Intel Xeon Gold 6226R CPU @ 2.9 GHz

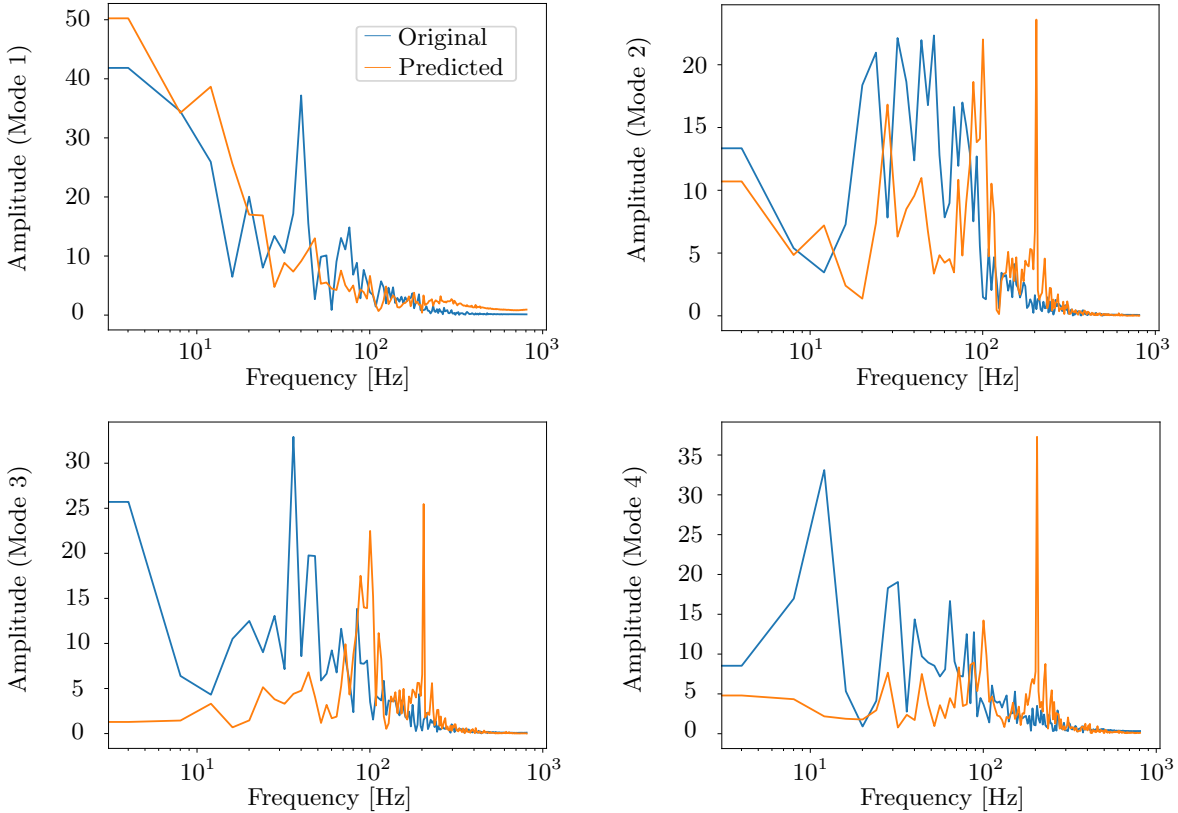


Figure 15: Power spectra for the temporal coefficients associated with the four most dominant POD velocity modes.

eterized with a novel value of the parameter, which was not used during the training of the model, with the predicted solution using the parametric 3D temporal convolution autoencoder reduced model. We emphasize that the prediction is made recursively and does not require supervision from the ground truth. Significant CPU time and memory reduction have been obtained since the reduced model does not demand high dimensional discretization of the numerical domain to produce an accurate solution. Results also showed that the model was able to accurately predict the flow field in the void region between particles, which is useful for many practical applications, including heat transfer analysis. However, the performance of the reduced model in the downstream region is limited. Despite this limitation, the overall vortex-shedding pattern in this region is captured.

Even though the application of the presented framework to a densely packed bed configuration remains to be explored, this study shows the potential of using deep learning to build reduced models for the prediction of flow fields in the void space in a packed bed configuration. In addition, the framework used in this study has potential applications in various engineering domains, such as heat exchangers. Future work will focus on improving the prediction accuracy in the downstream region, considering highly packed beds and extending the framework to include more simulation parameters.

Acknowledgments

Funded by the Deutsche Forschungsgemeinschaft (DFG, German Research Foundation) – Project-ID 422037413 – TRR 287.

Appendix A. Proper Orthogonal Decomposition

Proper orthogonal decomposition (POD) is a technique introduced by Lumley (1967) as a tool for extracting the dominant patterns in complex flow fields. The core of POD lies in capturing the essential dynamics of a system through the decomposition of high-dimensional data into a reduced set of orthogonal modes called POD modes.

Consider a set of snapshots denoted as $\mathbf{q}(t_m) \in \mathbb{R}^N$, where $m = 1, \dots, M$. The snapshot matrix $\mathbf{S} \in \mathbb{R}^{N \times M}$ is constructed by concatenating all the available snapshots across various time steps:

$$\mathbf{S} = [\mathbf{q}(t_1) \quad \mathbf{q}(t_2) \quad \cdots \quad \mathbf{q}(t_M)].$$

In the classical formulation introduced by Lumley (1967), the POD modes $\{\phi_1, \dots, \phi_r\} \subset \mathbb{R}^N$, where $r = \text{rank}(\mathbf{S})$, are defined as eigenvectors of the correlation matrix $\mathbf{S}\mathbf{S}^T \in \mathbb{R}^{N \times N}$, i.e.,

$$\mathbf{S}\mathbf{S}^T \Phi = \Phi \Lambda. \quad (19)$$

The given eigenvalue problem is closely related to the singular value decomposition (SVD) of the snapshot matrix \mathbf{S} , which reads

$$\mathbf{S} = \mathbf{U}\mathbf{\Sigma}\mathbf{V}^T, \quad (20)$$

where $\mathbf{U} \in \mathbb{R}^{N \times N}$ and $\mathbf{V} \in \mathbb{R}^{M \times M}$ are orthonormal matrices and $\mathbf{\Sigma} \in \mathbb{R}^{N \times M}$ is rectangular diagonal matrix with singular values $\sigma_1 \geq \sigma_2 \geq \dots \geq \sigma_r$. Using (20), the correlation matrix can be written as:

$$\mathbf{S}\mathbf{S}^T = \mathbf{U}\mathbf{\Sigma}\mathbf{V}^T\mathbf{V}\mathbf{\Sigma}\mathbf{U}^T = \mathbf{U}\mathbf{\Sigma}^2\mathbf{U}^T. \quad (21)$$

Right multiplying (21) with \mathbf{U} shows that the SVD of \mathbf{S} solves the eigenvalue problem of the correlation matrix, i.e., extracts the POD modes

$$\mathbf{S}\mathbf{S}^T\mathbf{U} = \mathbf{U}\mathbf{\Sigma}^2. \quad (22)$$

However, in many engineering applications, the direct computation of the POD modes becomes computationally intractable, especially when \mathbf{q}_i results from a high dimensional discretization of the numerical domain, i.e., $N \gg 1$. Therefore, Sirovich (1987) introduced the method of snapshots as a computationally efficient and tractable algorithm to extract the POD modes.

Once the POD modes have been determined, the quantity of interest $\mathbf{q}(t_m)$ can be approximated as a linear combination of the POD modes

$$\hat{\mathbf{q}}(t_m) \approx \sum_{i=1}^K a_i(t_m) \phi_i, \quad (23)$$

where a_i is the temporal coefficient associated with the POD mode ϕ_i at time step t_m . If we choose $K = r$, the approximation is exact, i.e., $\hat{\mathbf{q}}(t_m) = \mathbf{q}(t_m)$, while choosing $K < r$ results in $\hat{\mathbf{q}}(t_m)$ being a low rank approximation of $\mathbf{q}(t_m)$ in the subspace spanned by $\{\phi_1, \dots, \phi_K\}$. The accuracy of the approximation can be controlled such that

$$\epsilon = 1 - \frac{\sum_{i=1}^K \lambda_i}{\sum_{i=1}^r \lambda_i}, \quad (24)$$

is sufficiently small. Here, λ_i is the i -th eigenvalue of the correlation matrix $\mathbf{S}\mathbf{S}^T$ as indicated in (19), which is equivalent to the square of the corresponding singular value of \mathbf{S} as shown in (22).

References

- Martín Abadi. TensorFlow: A system for Large-Scale machine learning. In *12th USENIX Symposium on Operating Systems Design and Implementation (OSDI 16)*, pages 265–283, Savannah, GA, November 2016. USENIX Association. ISBN 978-1-931971-33-1.
- Saeed Akbari, Suraj Pawar, and Omer San. Numerical assessment of a nonintrusive surrogate model based on recurrent neural networks and proper orthogonal decomposition: Rayleigh Bénard convection. *International Journal of Computational Fluid Dynamics*, 36(7):599–617, aug 2022. doi: 10.1080/10618562.2022.2154918.
- Matteo Ambrosetti, Mauro Bracconi, Matteo Maestri, Gianpiero Groppi, and Enrico Tronconi. Packed foams for the intensification of catalytic processes: assessment of packing efficiency and pressure drop using a combined experimental and numerical approach. *Chemical Engineering Journal*, 382:122801, 2020. ISSN 1385-8947. doi: 10.1016/j.cej.2019.122801.
- Andrea J. Bader, Artin Afacan, Dave Sharp, and Karl T. Chuang. Effect of liquid-phase properties on separation efficiency in a randomly packed distillation column. *The Canadian Journal of Chemical Engineering*, 93(6):1119–1125, 2015. doi: 10.1002/cjce.22198.
- Hua Bai, Jörg Theuerkauf, Paul A. Gillis, and Paul M. Witt. A coupled DEM and CFD simulation of flow field and pressure drop in fixed bed reactor with randomly packed catalyst particles. *Industrial & Engineering Chemistry Research*, 48(8):4060–4074, 2009. doi: 10.1021/ie801548h.
- Mikhail Belkin and Partha Niyogi. Laplacian eigenmaps for dimensionality reduction and data representation. *Neural Computation*, 15(6):1373–1396, 2003. doi: 10.1162/089976603321780317.
- Peter Benner, Serkan Gugercin, and Karen Willcox. A survey of projection-based model reduction methods for parametric dynamical systems. *SIAM Review*, 57(4):483–531, 2015. doi: 10.1137/130932715.
- R Byron Bird. Transport phenomena. *Appl. Mech. Rev.*, 55(1):R1–R4, 2002. doi: 10.1002/aic.690070245.

- M. Braza, P. Chassaing, and H. Ha Minh. Numerical study and physical analysis of the pressure and velocity fields in the near wake of a circular cylinder. *Journal of Fluid Mechanics*, 165:79–130, 1986. doi: 10.1017/S0022112086003014.
- A. Elouali, T. Kousksou, T. El Rhafiki, S. Hamdaoui, M. Mahdaoui, A. Allouhi, and Y. Zeraouli. Physical models for packed bed: Sensible heat storage systems. *Journal of Energy Storage*, 23:69–78, 2019. ISSN 2352-152X. doi: 10.1016/j.est.2019.03.004.
- R. Fu, D. Xiao, I.M. Navon, F. Fang, L. Yang, C. Wang, and S. Cheng. A non-linear non-intrusive reduced order model of fluid flow by auto-encoder and self-attention deep learning methods. *International Journal for Numerical Methods in Engineering*, 124(13): 3087–3111, 2023. doi: <https://doi.org/10.1002/nme.7240>.
- Kai Fukami, Kazuto Hasegawa, Taichi Nakamura, Masaki Morimoto, and Koji Fukagata. Model order reduction with neural networks: Application to laminar and turbulent flows. *SN Computer Science*, 2(6), sep 2021. doi: 10.1007/s42979-021-00867-3.
- L. Geissbühler, V. Becattini, G. Zanganeh, S. Zavattoni, M. Barbato, A. Haselbacher, and A. Steinfeld. Pilot-scale demonstration of advanced adiabatic compressed air energy storage, part 1: Plant description and tests with sensible thermal-energy storage. *Journal of Energy Storage*, 17:129–139, 2018. ISSN 2352-152X. doi: 10.1016/j.est.2018.02.004.
- Chi Geng and JianXin Song. Human action recognition based on convolutional neural networks with a convolutional auto-encoder. In *Proceedings of the 2015 5th International Conference on Computer Sciences and Automation Engineering*, pages 933–938. Atlantis Press, 2016. ISBN 978-94-6252-156-8. doi: 10.2991/iccsae-15.2016.173.
- Xiaoxiao Guo, Wei Li, and Francesco Iorio. Convolutional neural networks for steady flow approximation. KDD '16, page 481–490, New York, NY, USA, 2016. Association for Computing Machinery. ISBN 9781450342322. doi: 10.1145/2939672.2939738.
- Kazuto Hasegawa, Kai Fukami, Takaaki Murata, and Koji Fukagata. Machine-learning-based reduced-order modeling for unsteady flows around bluff bodies of various shapes. *Theoretical and Computational Fluid Dynamics*, 34, 2020. doi: 10.1016/j.cma.2019.112766.
- Seyed Ali Hosseini, Hesam Safari, Nasser Darabiha, Dominique Thévenin, and Manfred Krafczyk. Hybrid lattice Boltzmann-finite difference model for low mach number combustion simulation. *Combustion and Flame*, 209:394–404, 2019. doi: 10.1016/j.combustflame.2019.07.041.
- Yuqing Hou, Hui Li, Hong Chen, Wei Wei, Jiayue Wang, and Yicang Huang. A novel deep U-Net-LSTM framework for time-sequenced hydrodynamics prediction of the suboff aff-8. *Engineering Applications of Computational Fluid Mechanics*, 16(1):630–645, 2022. doi: 10.1080/19942060.2022.2030802.
- Sergey Ioffe and Christian Szegedy. Batch normalization: Accelerating deep network training by reducing internal covariate shift. *CoRR*, abs/1502.03167, 2015.

- Diederik P. Kingma and Jimmy Ba. Adam: A method for stochastic optimization. In *Proceedings of the 3rd international conference on learning representations (ICLR)*. arXiv, 2014. doi: 10.48550/ARXIV.1412.6980.
- Mingyin Kou, Heng Zhou, Shengli Wu, and Yansong Shen. DEM simulation of cubical particle percolation in a packed bed. *Powder Technology*, 361:306–314, 2020. ISSN 0032-5910. doi: 10.1016/j.powtec.2019.08.012.
- Martin Kutscherauer, Sebastian Böcklein, Gerhard Mestl, Thomas Turek, and Gregor D. Wehinger. An improved contact modification routine for a computationally efficient CFD simulation of packed beds. *Chemical Engineering Journal Advances*, 9:100197, 2022. ISSN 2666-8211. doi: 10.1016/j.cej.2021.100197.
- Chia-Chang Lin, Wen-Tzong Liu, and Chung-Sung Tan. Removal of carbon dioxide by absorption in a rotating packed bed. *Industrial & Engineering Chemistry Research*, 42(11):2381–2386, 2003. doi: 10.1021/ie020669+.
- Hugo F. S. Lui and William R. Wolf. Construction of reduced-order models for fluid flows using deep feedforward neural networks. *Journal of Fluid Mechanics*, 872:963–994, jun 2019. doi: 10.1017/jfm.2019.358.
- Lumley. The structure of inhomogeneous turbulence. *Atmospheric Turbulence and Wave Propagation*, pages 166 – 178, 1967.
- A. Mjalled, L. Reineking, and M. Mönnigmann. Parametric data-driven reduced order model using neural networks and manifold-based interpolation. In *Proceedings of the 24th International Conference on Process Control, High Tatras*, page 168–173, 2023.
- Reza Namdar, Mohammadhassan Khodsiani, Hesameddin Safari, Tanya Neeraj, Seyed Ali Hosseini, Frank Beyrau, Benoît Fond, Dominique Thévenin, and Fathollah Varnik. Numerical study of convective heat transfer in static arrangements of particles with arbitrary shapes: A monolithic hybrid lattice boltzmann-finite difference-phase field solver. *Particuology*, 85:186–197, 2023. ISSN 1674-2001. doi: 10.1016/j.partic.2023.03.020.
- Pranshu Pant, Ruchit Doshi, Pranav Bahl, and Amir Barati Farimani. Deep learning for reduced order modelling and efficient temporal evolution of fluid simulations. *Physics of Fluids*, 33(10):107101, oct 2021. doi: 10.1063/5.0062546.
- S. Pawar, S. M. Rahman, H. Vaddireddy, O. San, A. Rasheed, and P. Vedula. A deep learning enabler for non-intrusive reduced order modeling of fluid flows. *Physics of Fluids*, 31(8):085101, 2019. ISSN 1070-6631. doi: 10.1063/1.5113494.
- Zheng Qi, Shibo Kuang, and Aibing Yu. Lattice Boltzmann investigation of non-newtonian fluid flow through a packed bed of uniform spheres. *Powder Technology*, 343:225–236, 2019. ISSN 0032-5910. doi: 10.1016/j.powtec.2018.11.046.
- Lucas Reineking, Jonas Fischer, Ali Mjalled, Enric Illana, Siegmund Wirtz, Viktor Scherer, and Martin Mönnigmann. Convective drying of wood chips: accelerating coupled DEM-CFD simulations with parametrized reduced intra-particle models. *Particuology*, 84, 2023. doi: 10.1016/j.partic.2023.03.012.

- D. E. Rumelhart, G. E. Hinton, and R. J. Williams. *Learning Internal Representations by Error Propagation*, page 318–362. MIT Press, Cambridge, MA, USA, 1986a. ISBN 026268053X.
- D. E. Rumelhart, Geoffrey E. Hinton, and Ronald J. Williams. Learning Representations by Back-propagating Errors. *Nature*, 323(6088):533–536, 1986b.
- Vinothkumar Sekar, Qinghua Jiang, Chang Shu, and Boo Cheong Khoo. Fast flow field prediction over airfoils using deep learning approach. *Physics of Fluids*, 31(5), 05 2019. ISSN 1070-6631. doi: 10.1063/1.5094943. 057103.
- Atul Sharma and V. Eswaran. Heat and fluid flow across a square cylinder in the two-dimensional laminar flow regime. *Numerical Heat Transfer, Part A: Applications*, 45(3): 247–269, 2004. doi: 10.1080/10407780490278562.
- Lawrence Sirovich. Turbulence and the Dynamics of coherent Structures. Part I: Coherent Structures. *Quarterly of applied Mathematics*, 45(3):561–571, 1987.
- A. Sohankar, C. Norberg, and L. Davidson. Numerical simulation of unsteady low-reynolds number flow around rectangular cylinders at incidence. *Journal of Wind Engineering and Industrial Aerodynamics*, 69-71:189–201, 1997. ISSN 0167-6105. doi: 10.1016/S0167-6105(97)00154-2. Proceedings of the 3rd International Colloquium on Bluff Body Aerodynamics and Applications.
- Jan Vierendeels, Bart Merci, and Erik Dick. Benchmark solutions for the natural convective heat transfer problem in a square cavity with large horizontal temperature differences. *International Journal of Numerical Methods for Heat & Fluid Flow*, 13(8):1057–1078, 2003. doi: 10.1108/09615530310501957.
- Qian Wang, Jan S. Hesthaven, and Deep Ray. Non-intrusive reduced order modeling of unsteady flows using artificial neural networks with application to a combustion problem. *Journal of Computational Physics*, 384:289–307, 2019. ISSN 0021-9991. doi: 10.1016/j.jcp.2019.01.031.
- Pin Wu, Junwu Sun, Xuting Chang, Wenjie Zhang, Rossella Arcucci, Yike Guo, and Christopher C. Pain. Data-driven reduced order model with temporal convolutional neural network. *Computer Methods in Applied Mechanics and Engineering*, 360:112766, 2020. ISSN 0045-7825. doi: 10.1016/j.cma.2019.112766.
- Jiayang Xu and Karthik Duraisamy. Multi-level convolutional autoencoder networks for parametric prediction of spatio-temporal dynamics. *Computer Methods in Applied Mechanics and Engineering*, 372:113379, 2020. ISSN 0045-7825. doi: 10.1016/j.cma.2020.113379.
- Junhai Zhai, Sufang Zhang, Junfen Chen, and Qiang He. Autoencoder and its various variants. In *2018 IEEE International Conference on Systems, Man, and Cybernetics (SMC)*, pages 415–419, 2018. doi: 10.1109/SMC.2018.00080.

Yiru Zhao, Bing Deng, Chen Shen, Yao Liu, Hongtao Lu, and Xian-Sheng Hua. Spatio-temporal autoencoder for video anomaly detection. In *Proceedings of the 25th ACM International Conference on Multimedia*, MM '17, page 1933–1941, New York, NY, USA, 2017. Association for Computing Machinery. ISBN 9781450349062. doi: 10.1145/3123266.3123451.

Tong Zhou and Yongbo Peng. Kernel principal component analysis-based gaussian process regression modelling for high-dimensional reliability analysis. *Computers and Structures*, 241:106358, 2020. ISSN 0045-7949. doi: 10.1016/j.compstruc.2020.106358. URL <https://www.sciencedirect.com/science/article/pii/S0045794920301619>.